nature communications

Article

https://doi.org/10.1038/s41467-024-54655-7

Chiral spin-liquid-like state in pyrochlore iridate thin films

Received: 28 March 2024

Accepted: 15 November 2024

Published online: 28 November 2024

Check for updates

Xiaoran Liu[1,2] ✉, Jong-Woo Kim[3], Yao Wang[4], Michael Terilli[2], Xun Jia[5,6], Mikhail Kareev[2], Shiyu Peng[1,7], Fangdi Wen[2], Tsung-Chi Wu[2], Huyongqing Chen[8], Wanzheng Hu[8,9,10], Mary H. Upton[3], Jungho Kim[3], Yongseong Choi[3], Daniel Haskel[3], Hongming Weng[1,7], Philip J. Ryan[3], Yue Cao[6], Yang Qi[4], Jiandong Guo[1,7] & Jak Chakhalian[2]

The pyrochlore iridates have become ideal platforms to unravel fascinating correlated and topological phenomena that stem from the intricate interplay among strong spin-orbit coupling, electronic correlations, lattice with geometric frustration, and itinerancy of the *5d* electrons. The all-in-all-out antiferromagnetic state, commonly considered as the magnetic ground state, can be dramatically altered in reduced dimensionality, leading to exotic or hidden quantum states inaccessible in bulk. Here, by means of magnetotransport, resonant elastic and inelastic x-ray scattering experiments, we discover an emergent quantum disordered state in (111) $Y_2Ir_2O_7$ thin films (thickness ≤30 nm) persisting down to 5 K, characterized by dispersionless magnetic excitations. The anomalous Hall effect observed below an onset temperature near 125 K corroborates the presence of chiral short-range spin configurations expressed in non-zero scalar spin chirality, breaking the macroscopic time-reversal symmetry. The origin of this chiral state is ascribed to the restoration of magnetic frustration on the pyrochlore lattice in lower dimensionality, where the competing exchange interactions together with enhanced quantum fluctuations suppress any long-range order and trigger spin-liquid-like behavior with degenerate ground-state manifold.

In the past decade, the field of emergent many-body phenomena in solids has undergone a paradigm shift driven by the convergence of two major streams of quantum materials: band topology and electron-electron interaction[1]. In heavy transition metal compounds with comparable strength of spin-orbit coupling (SOC) and on-site Coulomb repulsion, the electron band topology is intertwined with magnetism, leading to novel correlated topological phases with spontaneous time-reversal symmetry breaking[2–4]. Pyrochlore iridates $R_2Ir_2O_7$ (R = Y and rare-earth elements) are a representative model system that has received considerable attention for exploring the delicate balance between SOC, correlations, and the itinerancy of *5d* electrons embedded on the geometrically frustrated pyrochlore lattice. From theoretical viewpoint, extremely rich phase diagrams of $R_2Ir_2O_7$ have been constructed with a plethora of interesting correlated topological phenomena[5–16]. Recently, the link between topological properties and dimensionality has further inspired the predictions and

[1]Beijing National Laboratory for Condensed Matter Physics and Institute of Physics, Chinese Academy of Sciences, Beijing, China. [2]Department of Physics and Astronomy, Rutgers University, Piscataway, NJ, USA. [3]X-ray Science Division, Argonne National Laboratory, Lemont, IL, USA. [4]State Key Laboratory of Surface Physics and Department of Physics, Fudan University, Shanghai, China. [5]Multi-disciplinary Research Division, Institute of High Energy Physics, Chinese Academy of Sciences, Beijing, China. [6]Materials Science Division, Argonne National Laboratory, Lemont, IL, USA. [7]School of Physical Sciences, University of Chinese Academy of Sciences, Beijing, China. [8]Department of Physics, Boston University, Boston, MA, USA. [9]Division of Materials Science and Engineering, Boston University, Boston, MA, USA. [10]Photonics Center, Boston University, Boston, MA, USA. ✉e-mail: xiaoran.liu@iphy.ac.cn

search for emergent hidden quantum states that are only accessible in (111)-oriented thin films of pyrochlore iridates[17–27].

In bulk, the high temperature "parent" phase of $R_2Ir_2O_7$ is the Luttinger-Abrikosov-Beneslavskii (LAB) non-Fermi-liquid semimetal, with a quadratic band touching point located at the zone center[28–30]. At low temperatures, formation of magnetic long-range ordering (LRO) on the Ir sublattice can turn the LAB semimetal into various topological Weyl states[28]. The magnetic interactions between Ir^{4+} ions on the corner-sharing tetrahedral network are governed by two leading terms: antiferromagnetic (AFM) Heisenberg exchange and Dzyaloshinskii-Moriya (DM) interaction. The AFM interaction can induce strong frustration and lead to a highly degenerate spin-liquid ground state. In contrast, the DM interaction tends to lift the degeneracy and stabilize LRO with the peculiar all-in-all-out (AIAO) spin configuration[31–37] [Fig. 1b]. Furthermore, the inclusion of pseudo-dipolar interaction, single-ion anisotropy, or the variation of rare-earth R ion rapidly expands the phase space, stabilizing twelve symmetry-allowed $\mathbf{q} = 0$ spin configurations and their linear combinations as the plausible magnetic ground state[10,11,16,38].

In the quasi-two-dimensional (quasi-2D) limit, however, the tetrahedral network can be transformed into a thin (111)-oriented slab composed of several kagome and triangle atomic layers. In this case, one can envision how the competition among multiple AFM exchanges may restore strong frustration and stabilize an exotic short-range order with finite scalar spin chirality[39]. Conceptually, this novel magnetic state is akin to a chiral spin liquid (CSL), where fluctuating spin dimers cover the entire pyrochlore slab and break the global time-reversal symmetry[40,41]. As such, it is interesting to explore the challenging question of the true magnetic ground state of pyrochlore iridates on the thin (111)-oriented slab.

For this purpose, we have developed a set of high-quality (111) $Y_2Ir_2O_7$ films using the in-situ solid phase epitaxy method[42]. By means of resonant x-ray magnetic scattering techniques and magneto-transport measurements, we have discovered the formation of $\mathbf{q} = 0$ AFM LRO in 100 nm (111) $Y_2Ir_2O_7$ films at a Néel temperature near 140 K. Surprisingly, the LRO is absent in thin films (≤30 nm). In this quasi-2D limit, a novel CSL state with anomalous Hall effect (AHE) appears below a characteristic temperature around 135 K, stemming from the fluctuating non-coplanar spin textures with non-zero chirality. In sharp contrast to the dispersive magnon mode observed in bulk crystals and predicted from the linear spin-wave theory, the CSL state exhibits spin-gapped but dispersionless spectrum of magnetic excitations. Our findings highlight the previously unexplored role of dimensional confinement to stabilize emergent quantum states in thin slabs of pyrochlore iridates for the first time.

Results

It is generally recognized that upon lowering the temperature, all $R_2Ir_2O_7$ except for R = Pr undergo a metal-to-insulator/semimetal transition concurrently with the AFM phase transition[43–47]. In particular, since bulk $Y_2Ir_2O_7$ shows the highest Néel temperature ~150 K and has no f-electron moments on the Y sublattice, it serves as an ideal playground to explore the intrinsic magnetism of the Ir^{4+} sublattice. Despite active experimental efforts, inconsistent results on the nature

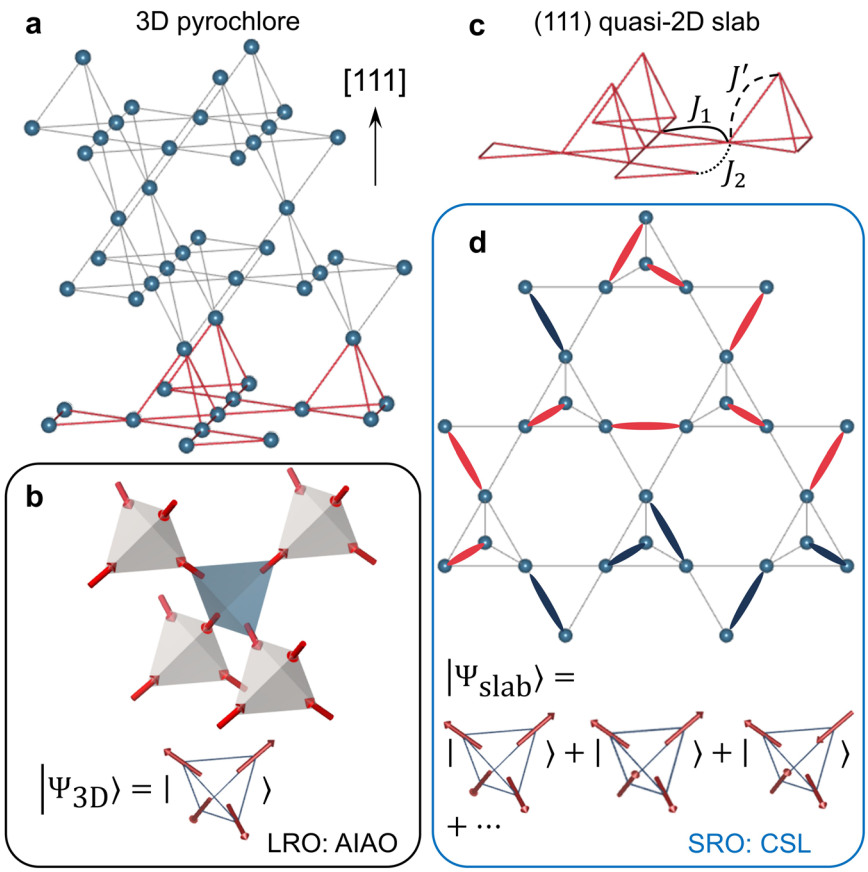

Fig. 1 | Schematics of exotic magnetism on (111) $Y_2Ir_2O_7$ lattice. a 3D pyrochlore framework constructed by Ir atoms. **b** Long-range ordering with the AIAO antiferromagnetic spin configuration on Ir sublattice. **c** (111) quasi-2D slab of pyrochlore lattice composed of alternating kagome and triangle atomic layers. J_1 (J_2) represents the Ir nearest-neighbor (next-nearest-neighbor) interaction within the kagome layers, while J' the nearest-neighbor interaction between kagome and triangle layers. **d** A possible snapshot of the chiral spin liquid configuration on (111) quasi-2D pyrochlore slab. The Ir spins pair up forming dimers covering the entire lattice. The two spin directions in one dimer can be either the same (red dimer: both towards or away from the center of tetrahedra) or opposite (blue dimer: one towards and one away from the center of tetrahedra).

https://doi.org/10.1038/s41467-024-54655-7

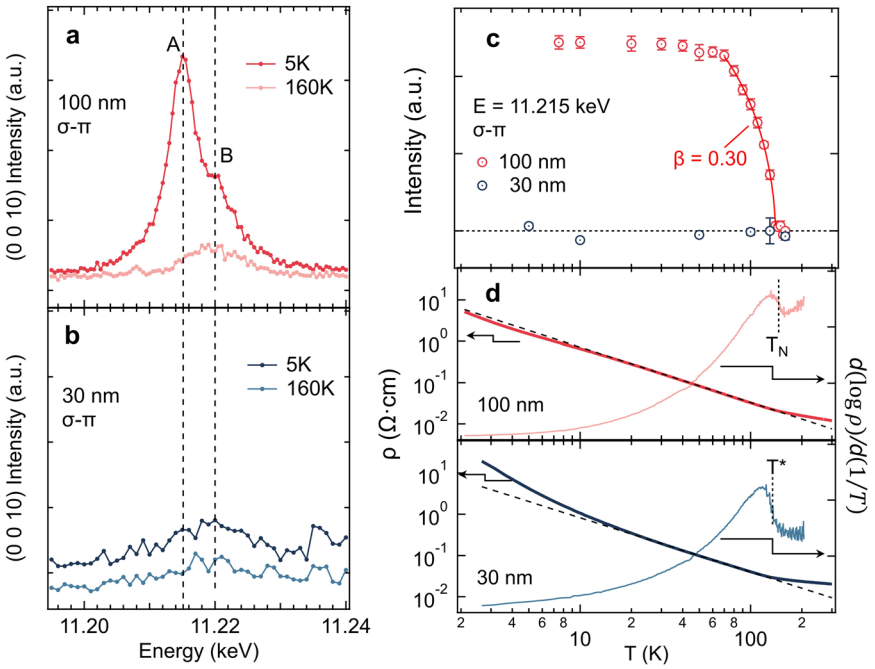

Fig. 2 | Magnetic phase transition in 100 nm and 30 nm (111) $Y_2Ir_2O_7$ films. Resonance profiles of the magnetic (0 0 10) reflection near Ir L_3 edge in the σ–π channel for (**a**) 100 nm and (**b**) 30 nm $Y_2Ir_2O_7$ films. A special azimuthal alignment which includes setting the [110] axis of the $Y_2Ir_2O_7$ films perpendicular to the scattering plane allows for effectively suppressing the ATS contribution and leaving the RMS signal dominant in the σ–π channel[32]. Peak A at 11.215 keV represents the RMS signal, which is significantly enhanced at 5 K in the long-range antiferromagnetic state. Peak B at 11.22 keV is due to the leakage of ATS that is dominant in the σ–σ channel. **c** Temperature dependence of the integrated intensity of magnetic (0 0 10) reflection for 100 nm (red) and 30 nm (blue) $Y_2Ir_2O_7$ films. The transition temperature $T_N \approx 140$ K and the critical exponent $\beta \approx 0.30$ of 100 nm sample are extracted from the data following the relationship $I \propto M^2 \propto (1-\frac{T}{T_N})^{2\beta}$. The error bars refer to the standard deviation of the integrated intensity calculated with a Gaussian function. **d** Temperature dependence of the resistivity of 100 nm (red) and 30 nm (blue) samples, which exhibit a "kink" behavior at around 145 K and 135 K, respectively. The black dashed lines are power-law fits ($\rho \propto T^{-\alpha}$) of the data between 100 and 20 K, with the power index $\alpha \sim 1.3$ (1.4) for 100 nm (30 nm) sample.

of the ground state have been reported. For instance, well-defined oscillations of single frequency were observed in muon spin resonance/relaxation spectra, indicating the formation of LRO[48]. But meanwhile, neutron powder diffraction data yielded no sign of magnetic peaks at low temperatures, attributed to high neutron absorption of Ir[49]. With the availability of high-quality single-crystalline films, we use the resonant X-ray diffraction (RXD) at the Ir L_3 edge to address this fundamental question.

The AIAO spin structure is a $\mathbf{q} = 0$ LRO, which triggers charge-forbidden reflections such as (0 0 4n+2) visible in the resonant magnetic scattering (RMS). However, due to the local trigonal distortion of the IrO_6 octahedra, the anisotropic tensor susceptibility (ATS) scattering is also attributed to the (0 0 4n+2) reflections[50]. As seen in Fig. 2a, in 100 nm $Y_2Ir_2O_7$, the magnetic Bragg signal is clearly observed at 5 K in the energy spectra of (0 0 10) reflection at peak A ($E = 11.215$ keV); the signal gradually diminishes to zero at 160 K. The hump feature at peak B ($E = 11.22$ keV) is a leakage of the ATS scattering into the σ–π channel, and its intensity barely varies with temperature (Supplementary Fig. 2). The temperature dependence of the (0 0 10) integrated intensity indicates the onset of magnetic phase transition near 140 K in 100 nm $Y_2Ir_2O_7$ [Fig. 2c]. These observations are in good agreement with the reported bulk value, demonstrating the establishment of LRO on the Ir sublattice[48]. A power-law fit of the scattered intensities in the vicinity of transition transition, $I \propto M^2 \propto (1-\frac{T}{T_N})^{2\beta}$ yields the critical exponent $\beta \approx 0.30$, falling into the 3D Ising universality class consistent with the AIAO spin configuration[13].

In stark contrast, direct examination of Fig. 2b immediately reveals that, other than the small leakage of ATS in the σ–π scattering channel, the RMS signal is no longer detectable in 30 nm $Y_2Ir_2O_7$ in a wide range of temperatures down to 5 K! Moreover, the absence of the expected magnetic scattering signal is verified on the set of (0 0 4n+2) reflections. A potential sample quality issue is ruled out, as the charge scattering peaks allowed for the pyrochlore lattice and the presence of characteristic ATS contributions are all detected [see Supplementary Figs. 1 and 2 for more details]. On the other hand, the X-ray magnetic circular dichroism (XMCD) spectra at 4 K have shown that the averaged net magnetic moment per Ir^{4+} ion is ~0.023(4) μ_B/Ir [Supplementary Fig. 3]. This is remarkably lower than the expected local moment of about 0.33 μ_B/Ir for the $J_{\text{eff}} = 1/2$ configuration[49], indicating an unusual paramagnetic (PM) behavior in 30 nm $Y_2Ir_2O_7$ even under 6 T magnetic field, where the local moments of Ir persistently fluctuate at low temperatures.

Next, we focus on the magneto-transport response of our (111)-oriented films. In bulk $Y_2Ir_2O_7$, the PM to AFM transition manifests itself as a "kink" on the temperature-dependent resistivity curve due to the inclusion of additional scattering channels from the long-range ordered spins. As seen in Fig. 2d, both films exhibit a semiconducting behavior with the kink feature on the ρ(T) curve. The kink of 100 nm $Y_2Ir_2O_7$ indeed appears near 145 K, coinciding with the Néel temperature T_N obtained from our magnetic scattering data [Fig. 2d, upper panel]. Surprisingly, the kink is also present in 30 nm $Y_2Ir_2O_7$ near $T^* \approx 135$ K [Fig. 2d, bottom panel], which signals the existence of a hidden order not captured by magnetic scattering.

The AHE is a direct and macroscopic probe of time-reversal symmetry in quantum antiferromagnets[4]. Our Hall transport data reveal the presence of distinct AHE at zero magnetic fields for both $Y_2Ir_2O_7$ films, signifying that the time-reversal symmetry is spontaneously broken at low temperatures [Fig. 3a, b]. Specifically, the transverse resistivity ρ_{xy} of 100 nm $Y_2Ir_2O_7$ displays a clear hysteresis loop right below the Néel temperature. For 30 nm $Y_2Ir_2O_7$, despite the absence of LRO, non-zero spontaneous Hall resistivity starts to emerge at 125 K, slightly below the characteristic temperature T^* obtained from

https://doi.org/10.1038/s41467-024-54655-7

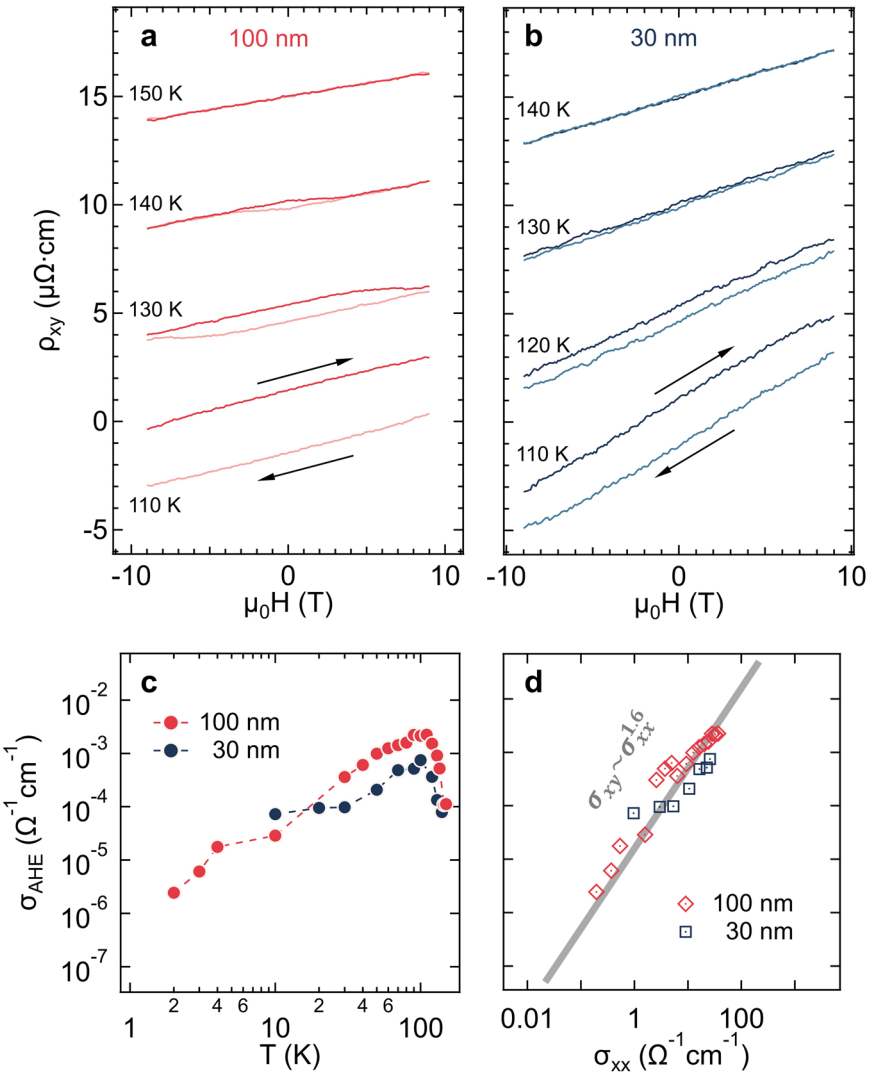

Fig. 3 | Anomalous Hall effect. Evolution of the transverse magneto-resistivity ρ_{xy} measured at a set of temperatures across (**a**) T_N of 100 nm and (**b**) T^* of 30 nm sample. Each branch of the curve (in light or heavy color) is obtained after field cooling, with an black arrow showing the corresponding scan direction. For clarity, the center of curve at each temperature is offset by 5 μΩ · cm. **c** Temperature dependence of the spontaneous Hall conductivity σ_{AHE} of 100 nm and 30 nm $Y_2Ir_2O_7$ films. **d** The scaling relationship between σ_{AHE} and σ_{xx} of $Y_2Ir_2O_7$ films.

the longitudinal ρ_{xx}(T) curve. It is also worth noting that the coercive fields of both samples increase rapidly as temperature decreases, making only a small portion of the loops visible [see "Methods" and Supplementary Figs. 5 and 6].

In addition, both films exhibit a non-monotonic temperature dependence of spontaneous Hall conductivity σ_{AHE} [Fig. 3c]. For 100 nm $Y_2Ir_2O_7$, the emergence of non-zero σ_{AHE} concurrently with the onset of the AIAO AFM order agrees with the theoretical prediction for the formation of Weyl semimetallic state in (111) pyrochlore iridate films[17,18,20]. Here, the incomplete cancellation of the Chern vectors over all Weyl pairs triggers an intrinsic AHE, as demonstrated recently in $Eu_2Ir_2O_7$ films[27]. Notably, symmetry analysis based on magnetic group theory strictly enforces zero scalar spin chirality for the AIAO configuration[51]. The non-monotonic σ_{AHE}(T) behavior (i.e., σ_{AHE} first increases to the maximum and gradually decreases on cooling) in 100 nm $Y_2Ir_2O_7$ thus reflects the evolution of the Berry curvatures in momentum-space, due to the motion of the Weyl nodes with decreasing temperatures[15]. Nevertheless, it is noteworthy that while in $Eu_2Ir_2O_7$ film, σ_{AHE} tends to level off to a finite value, σ_{AHE} of $Y_2Ir_2O_7$ is significantly suppressed as approaching the base temperature. This might indicate the tendency of annihilation of the Weyl pairs when reaching the edge of the Brillouin zone on approaching its ground state [Supplementary Fig. 7].

In contrast, because of the absence of LRO in 30 nm $Y_2Ir_2O_7$, it precludes the formation of Weyl nodes in this film. Meanwhile, the minute averaged magnetization obtained from XMCD at the Ir L-edge under 6 T excludes the origin of AHE from aligned moments in a conventional ferromagnet or a spin glass [Supplementary Fig. 3]. These findings strongly imply the presence of a chiral spin-liquid-like state below 125 K, with σ_{AHE} directly measuring the scalar spin chirality averaged over all short-range non-coplanar configurations[40].

Next, we explore the scaling relation between the longitudinal conductivity σ_{xx} and the σ_{AHE}. Conventionally, this relationship can be divided into three empirical regimes based on the value of σ_{xx}[52,53]. As depicted in Fig. 3d, both $Y_2Ir_2O_7$ films belong to the bad-metal-hopping regime, where σ_{AHE} decreases as σ_{xx} decreases, following the universal scaling of $\sigma_{xy} \sim \sigma_{xx}^{1.6}$ at temperatures below 100 K. Although the fundamental mechanism for the hopping regime is beyond resent theoretical framework and remains an open issue, this scaling behavior is indicative of complicated interplay between the intrinsic (i.e., the Berry-phase mechanism) and extrinsic (e.g., the side-jump scattering, inelastic scattering events, and higher-order perturbative terms) contributions[53].

https://doi.org/10.1038/s41467-024-54655-7

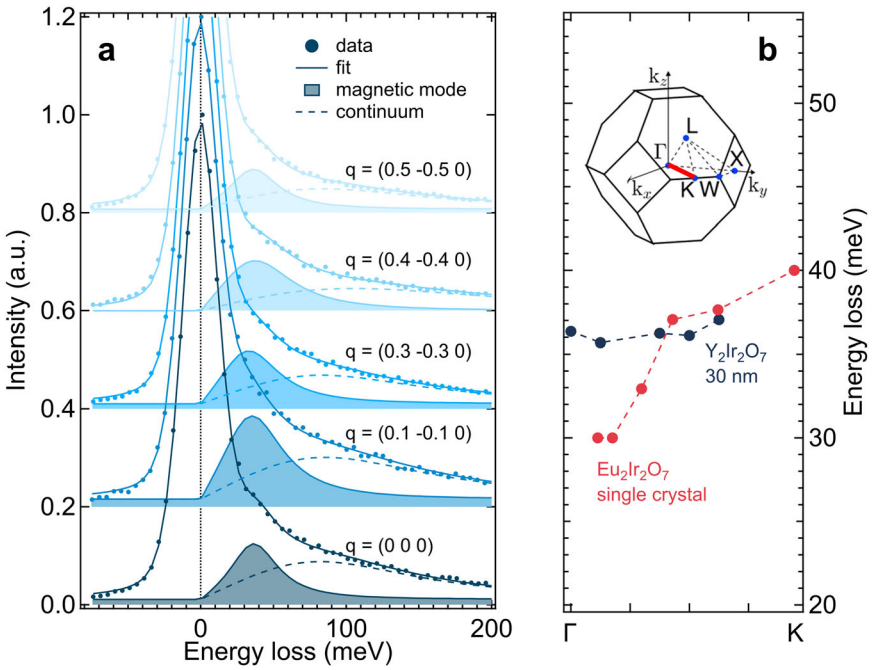

Fig. 4 | Magnetic excitation in 30 nm $Y_2Ir_2O_7$ film. a The stacking RIXS spectra along the Γ-K direction recorded at 10 K. The data (solid dots) are normalized with respect to the elastic scattering peak at 0 meV. Fitting of each spectrum yields the elastic background (solid curve), inelastic peak from the magnetic excitation (shadowed curve), and inelastic background continuum (dashed curve). **b** The extracted dispersion of magnetic excitation in 30 nm $Y_2Ir_2O_7$ film along the Γ-K direction. The inset illustrates the Brillouin zone with notations for high-symmetry positions. For comparison, the dispersive magnon reported in $Eu_2Ir_2O_7$ bulk crystal[54] with the AIAO LRO is plotted together on the figure.

In the presence of the CSL state in 30 nm $Y_2Ir_2O_7$, one can also anticipate the breakdown of classical spin-wave theory, as the spin excitations may exhibit marked deviations from the magnon modes of the bulk. In single crystals of pyrochlore iridates with the AIAO magnetic ground state, dispersive magnon modes with a spin gap of 25 meV and 28 meV have been probed by resonant inelastic X-ray scattering (RIXS) in $Sm_2Ir_2O_7$[33] and $Eu_2Ir_2O_7$[54]. Figure 4a demonstrates a set of RIXS spectra taken on 30 nm $Y_2Ir_2O_7$ at 10 K, with the energy loss range below 300 meV taken along the Γ-K direction of the Brillouin zone. The overall spectrum is composed of several distinct contributions. These include a peak at zero energy due to elastic scattering (solid curve) and two other peaks next to the elastic line (shadowed curve and dashed curve). The mode associated with the shadowed peak has an energy close to the spin gap observed in other pyrochlore iridates and is interpreted as a magnetic excitation. The dashed peak represents a particle-hole continuum that is incoherent.

The overall dispersion of the magnetic excitation of 30 nm $Y_2Ir_2O_7$ is shown in Fig. 4b. As immediately seen, it exhibits a surprisingly dispersionless feature over a momentum range larger than half Brillouin zone along the Γ-K direction. This unusual behavior is in sharp contrast to the previously reported RIXS data on pyrochlore iridates with the AIAO LRO, where gapped and dispersive magnon modes have been observed in the energy range from 20 meV to 40 meV along this direction[33,54]. Such a dispersionless magnetic excitation observed in 30 nm $Y_2Ir_2O_7$ necessitates a fundamentally different magnetic Hamiltonian in the quasi-2D case. While the exact form is unknown, the CSL state is plausibly stabilized due to the competition among multiple exchange interactions, melting the LRO and generating chiral spin textures imposed on the triangle and kagome structural units.

Discussion

The CSL state breaks the time-reversal symmetry, while remains magnetically disordered and entangled, fluctuating among the massively degenerate states[40]. For bulk pyrochlore iridates, the Ir twelve types of $\mathbf{q} = 0$ magnetic basis vectors ψ_i are categorized into four irreducible representations $\Gamma_{3,5,7,9}$ (Supplementary Fig. 8). Notably, to break the macroscopic time-reversal symmetry, only those six bases under Γ_9 are allowed to generate nonvanishing scalar spin chirality based on the multipole cluster theory[51]. In this sense, the overall wave function of the CSL in 30 nm $Y_2Ir_2O_7$ must include spin configurations containing these chiral bases, such as “two-in-two-out”, “three-in-one-out”, and/or other linearly combined ones, which is analogous to the Pr spin configurations in the metallic CSL state of $Pr_2Ir_2O_7$[44].

On the other hand, theoretical calculations reveal that the spin configurations of pyrochlore iridates are located very close in energy, within several meV[6,10]. This, in turn, implies the possibility of interconversion among the magnetic states by tuning the magnitudes of direct and indirect hopping between the Ir atoms[11,16,38,55]. Based on this observation, we speculate that in approaching the quasi-2D limit, truncation of the pyrochlore lattice along the (111) orientation and enhanced fluctuations rescale the relative strength of hopping and magnetic interactions, leading to a degenerate ground-state manifold. Figure 1d provides one of the plausible snapshots of the CSL state in 30 nm $Y_2Ir_2O_7$, where red and blue dimers denote the distribution of fluctuating short-range spin textures.

In summary, we unravel the abnormally “fragile” nature of the AIAO order and unlock a fresh region that has not been recognized on the global phase diagram of pyrochlore iridates. Moreover, the emergence of the CSL state enables new opportunities to explore other exotic quantum phases proposed for pyrochlore iridates, particularly quantum nematic[55], axion insulator[9], and unconventional superconductivity[22]. Future experiments at milli-Kelvin temperature and ultra-high magnetic field are essential to verify if the dynamic CSL state can persist or if the quantum-order-by-disorder mechanism eventually prevails and selects a static configuration.

Methods

Sample fabrication

The (111) oriented $Y_2Ir_2O_7$ thin films were fabricated on 5×5 mm^2 (111) yttria-doped ZrO_2 (YSZ) substrates by pulsed laser deposition. Ir-rich phase-mixed ceramic targets (Y:Ir = 1:3) were ablated using a KrF excimer laser ($\lambda = 248$ nm, energy density ~5 J/cm^2) with a repetition rate of 10 Hz. The deposition was first carried out at a substrate temperature of 450 °C, under 100 mTorr atmosphere composed of Ar and O_2 gases (partial pressure ratio, Ar:O_2 = 10:1). Amorphous film with the proper stoichiometry was obtained from this stage. Then the film was post-annealed inside the chamber at 950 °C under 500 Torr atmosphere of pure O_2 for 15–20 min, followed by cooling to room temperature. High-quality single crystalline film was eventually achieved.

Transport measurements

The electrical transport measurements were performed in a 9 T physical property measurement system (PPMS, Quantum Design) with the 4-point contact method. The magnetic field was applied along the [111] direction, and the current was driven along the [1$\bar{1}$0] direction. In particular, due to the extremely large coercivity, the magnetotransport at each temperature was measured in the following procedures. First, +9 T was applied at 150 K and the sample was field cooled to the desired temperature. The resistance was measured by sweeping field from +9 to −9 T. Then, sample was heated to 150 K (to quench any magnetic ordering), and cooled back to the same temperature, after which the resistance was measured again by sweeping field from −9 to +9 T. Symmetrization (anti-symmetrization) was further applied using these two branches on the longitudinal (transverse) resistance to achieve pure signal from the magnetoresistance (the Hall effect).

Resonant x-ray diffraction

The RXD experiments were performed at beamline 6-ID-B of the Advanced Photon Source in Argonne National Laboratory using a 6-circle diffractometer. The (111) $Y_2Ir_2O_7$ films were mounted in a close-cycle displex such that the in-plane [1$\bar{1}$0] direction was along the x-rays, and the [110] direction was aligned perpendicular to the scattering plane. The incident beam was linearly polarized perpendicular to the scattering plane (σ), with energy tuned around the Ir L_3 absorption edge. A PG (008) analyzer was used to filter the polarization of the scattered x-rays, leading to two detection channels, σ–σ and σ–π. The signal of resonant magnetic scattering can be effectively probed in the σ–π channel.

X-ray magnetic circular dichroism spectra

The resonant XMCD experiments were performed at beamline 4-ID-D of the Advanced Photon Source at Argonne National Laboratory. X-ray absorption spectra around Ir L_3 and L_2 edges were collected with left- and right-circularly polarized beams at normal incidence (k // [111]) to obtain the XMCD spectra. To exclude any artifact, XMCD spectra were measured in both positive and negative external field. In case of large magnetic coercivity, the measurements were conducted in two ways for comparison. (1) XMCD was recorded after sample was +6 T field cooled to 4 K; then sample was heated to 150 K (to quench any magnetic ordering) and cooled back to 4 K with −6 T field, after which XMCD was recorded. (2) XMCD was recorded after sample was +6 T field cooled to 4 K. Then the magnetic field was directly swept to −6 T at 4 K, after which XMCD was recorded. The spectra obtained in both ways are almost identical.

Resonant inelastic x-ray scattering

RIXS measurements were taken at beamline 27-ID-B of Advanced Photon Source. The incoming photon energy was tuned to the Ir L_3 pre-edge (11.215 keV) with 28 meV resolution (FWHM) to enhance the magnetic scattering cross-section. Measurements on thin films of several tens' nm at such a hard x-ray facility imposed several constraints on the sample geometry: (a) grazing-incident geometry to guarantee the maximal footprint of x-ray beams on the film, enhancing the overall scattering signal; (b) $2\theta \approx 90°$ to minimize the elastic scattering signal and to purify the magnetic signal. Furthermore, the magnetic signal was enhanced by selecting a peak which was structurally forbidden but magnetically allowed. As a result, measurements were taken around the (5 12 −1) peak. To obtain the exact information of these peaks, the elastic line was fitted to a Voigt function with a resolution determined at Γ point. The inelastic peaks were fitted to anti-symmetrized Lorentzian line shapes of the form: $S(Q,\omega) = \frac{A}{2\pi(1-exp(\frac{\omega}{k_BT}))}\gamma(\frac{1}{(\omega-\omega_0)^2+(\gamma/2)^2} + \frac{1}{(\omega+\omega_0)^2+(\gamma/2)^2})$, where A is the peak amplitutde, $\frac{1}{1-exp(\frac{\omega}{k_BT})}$ is the Bose factor, γ is the peak width, and ω_0 is the peak position.

Data availability

All data that support the findings of this study are available from the corresponding author on request.

References

1. Tokura, Y., Kawasaki, M. & Nagaosa, N. Emergent functions of quantum materials. *Nat. Phys.* **13**, 1056 (2017).
2. Witczak-Krempa, W., Chen, G., Kim, Y. B. & Balents, L. Correlated quantum phenomena in the strong spin-orbit regime. *Annu. Rev. Condens. Matter Phys.* **5**, 57–82 (2014).
3. Nenno, D., Garcia, C., Gooth, J., Felser, C. & Narang, P. Axion physics in condensed-matter systems. *Nat. Rev. Phys.* **2**, 682 (2020).
4. Smejkal, L., MacDonald, A., Sinova, J., Nakatsuji, S. & Jungwirth, T. Anomalous Hall antiferromagnets. *Nat. Rev. Mater.* **7**, 482 (2022).
5. Pesin, D. & Balents, L. Mott Physics and band topology in materials with strong spin-orbit interaction. *Nat. Phys.* **6**, 376–381 (2010).
6. Wan, X., Turner, A. M., Vishwanath, A. & Savrasov, S. Y. Topological semimetal and Fermi-arc surface states in the electronic structure of pyrochlore iridates. *Phys. Rev. B* **83**, 205101 (2011).
7. Wang, R., Go, A. & Millis, A. J. Electron interactions, spin-orbit coupling, and intersite correlations in pyrochlore iridates. *Phys. Rev. B* **95**, 045133 (2017).
8. Go, A., Witczak-Krempa, W., Jeon, G., Park, K. & Kim, Y. Correlation effects on 3D topological phases: from bulk to boundary. *Phys. Rev. Lett.* **109**, 066401 (2012).
9. Varnava, N. & Vanderbilt, D. Surfaces of axion insulators. *Phys. Rev. B* **98**, 245117 (2018).
10. Wang, Y., Weng, H., Fu, L. & Dai, X. Noncollinear magnetic structure and multipolar order in $Eu_2Ir_2O_7$. *Phys. Rev. Lett.* **119**, 187203 (2017).
11. Ladovrechis, K., Meng, T. & Roy, B. Competing magnetic orders and multipolar Weyl fermions in 227 pyrochlore iridates. *Phys. Rev. B* **103**, L241116 (2021).
12. Shinaoka, H., Hoshino, S., Troyer, M. & Werner, P. Phase diagram of pyrochlore iridates: all-in-all-out magnetic ordering and non-Fermi-liquid properties. *Phys. Rev. Lett.* **115**, 156401 (2015).
13. Savary, L., Moon, E. & Balents, L. New types of quantum criticality in the pyrochlore iridates. *Phys. Rev. X* **4**, 041027 (2014).
14. Hwang, K., Trivedi, N. & Randeria, M. Topological magnons with nodal-line and triple-point degeneracies: implications for thermal Hall effect in pyrochlore iridates. *Phys. Rev. Lett.* **125**, 047203 (2020).
15. Yamaji, Y. & Imada, M. Metallic interface emerging at magnetic domain wall of antiferromagnetic insulator: fate of extinct Weyl electrons. *Phys. Rev. X* **4**, 021035 (2014).
16. Witczak-Krempa, W. & Kim, Y. B. Topological and magnetic phases of interacting electrons in the pyrochlore iridates. *Phys. Rev. B* **85**, 045124 (2012).

17. Hu, X., Rüegg, A. & Fiete, G. A. Topological phases in layered pyrochlore oxide thin films along the [111] direction. *Phys. Rev. B* **86**, 235141 (2012).
18. Yang, B.-J. & Nagaosa, N. Emergent topological phenomena in thin films of pyrochlore iridates. *Phys. Rev. Lett.* **112**, 246402 (2014).
19. Bergholtz, E., Liu, Z., Trescher, M., Moessner, R. & Udagawa, M. Topology and interactions in a frustrated slab: tuning from Weyl semimetals to $C > 1$ fractional Chern insulators. *Phys. Rev. Lett.* **114**, 016806 (2015).
20. Hwang, K. & Kim, Y. Theory of multifarious quantum phases and large anomalous Hall effect in pyrochlore iridate thin films. *Sci. Rep.* **6**, 30017 (2016).
21. Chen, Q., Hung, H., Hu, X. & Fiete, G. A. Correlation effects in pyrochlore iridate thin films grown along the [111] direction. *Phys. Rev. B* **92**, 085145 (2015).
22. Laurell, P. & Fiete, G. A. Topological magnon bands and unconventional superconductivity in pyrochlore iridate thin films. *Phys. Rev. Lett.* **118**, 177201 (2017).
23. Ohtsuki, T. et al. Strain-induced spontaneous Hall effect in an epitaxial thin film of a Luttinger semimetal. *Proc. Natl. Acad. Sci. USA* **116**, 8803–8808 (2019).
24. Guo, L. et al. Spontaneous Hall effect enhanced by local Ir moments in epitaxial $Pr_2Ir_2O_7$ thin films. *Phys. Rev. B* **101**, 104405 (2020).
25. Kim, W. et al. Strain engineering of the magnetic multipole moments and anomalous Hall effect in pyrochlore iridate thin films. *Sci. Adv.* **6**, eabb1539 (2020).
26. Li, Y. et al. Correlated magnetic Weyl semimetal state in strained $Pr_2Ir_2O_7$. *Adv. Mater.* **33**, 2008528 (2021).
27. Liu, X. et al. Magnetic Weyl semimetallic phase in thin films of $Eu_2Ir_2O_7$. *Phys. Rev. Lett.* **127**, 277204 (2021).
28. Moon, E., Xu, C., Kim, Y. & Balents, L. Non-Fermi-liquid and topological states with strong spin-orbit coupling. *Phys. Rev. Lett.* **111**, 206401 (2013).
29. Kondo, T. et al. Quadratic Fermi node in a 3D strongly correlated semimetal. *Nat. Commun.* **6**, 10042 (2015).
30. Nakayama, M. et al. Slater to Mott crossover in the metal to insulator transition of $Nd_2Ir_2O_7$. *Phys. Rev. Lett.* **117**, 056403 (2016).
31. Elhajal, M., Canals, B., Sunyer, R. & Lacroix, C. Ordering in the pyrochlore antiferromagnet due to Dzyaloshinsky-Moriya interactions. *Phys. Rev. B* **71**, 094420 (2005).
32. Sagayama, H. et al. Determination of long-range all-in-all-out ordering of Ir^{4+} moments in a pyrochlore iridate $Eu_2Ir_2O_7$ by resonant x-ray diffraction. *Phys. Rev. B* **87**, 100403(R) (2013).
33. Donnerer, C. et al. All-in-all-out magnetic order and propagating spin waves in $Sm_2Ir_2O_7$. *Phys. Rev. Lett.* **117**, 037201 (2016).
34. Tomiyasu, K. et al. Emergence of magnetic long-range order in frustrated pyrochlore $Nd_2Ir_2O_7$ with metal-insulator transition. *J. Phys. Soc. Jpn.* **81**, 034709 (2012).
35. Lefrancois, E. et al. Anisotropy-tuned magnetic order in pyrochlore iridates. *Phys. Rev. Lett.* **114**, 247202 (2015).
36. Disseler, S. Direct evidence for the all-in/all-out magnetic structure in the pyrochlore ir dates from muon spin relaxation. *Phys. Rev. B* **89**, 140413(R) (2014).
37. Lefrancois, E. et al. Fragmentation in spin ice from magnetic charge injection. *Nat. Commun.* **8**, 209 (2017).
38. Chen, G. & Wang, X. Electron quasi-itinerancy intertwined with quantum order by disorder in pyrochlore iridate magnetism. *Phys. Rev. Research* **2**, 043273 (2020).
39. Kawamura, H. & Arimori, T. Chiral Kosterlitz-Thouless transition in the frustrated Heisenberg antiferromagnet on a pyrochlore slab. *Phys. Rev. Lett.* **88**, 077202 (2002).
40. Wen, X., Wilczek, F. & Zee, A. Chiral spin states and superconductivity. *Phys. Rev. B* **39**, 11413 (1989).
41. Messio, L., Bieri, S., Lhuillier, C. & Bernu, B. Chiral spin liquid on a Kagome antiferromagnet induced by the Dzyaloshinskii-Moriya interaction. *Phys. Rev. Lett.* **118**, 267201 (2017).
42. Liu, X. et al. In-situ fabrication and transport properties of (111) $Y_2Ir_2O_7$ epitaxial thin film. *Appl. Phys. Lett.* **117**, 041903 (2020).
43. Gardner, J., Gingras, M. & Greedan, J. Magnetic pyrochlore oxides. *Rev. Mod. Phys.* **82**, 53 (2010).
44. Machida, Y., Nakatsuji, S., Onoda, S., Tayama, T. & Sakakibara, T. Time-reversal symmetry breaking and spontaneous Hall effect without magnetic dipole order. *Nature* **463**, 210 (2010).
45. Matsuhira, K., Wakeshima, M., Hinatsu, Y. & Takagi, S. Metal-insulator transition in pyrochlore oxides $Ln_2Ir_2O_7$. *J. Phys. Soc. Jpn.* **80**, 094701 (2011).
46. Ueda, K., Fujioka, J. & Tokura, Y. Variation of optical conductivity spectra in the course of bandwidth-controlled metal-insulator transitions in pyrochlore iridates. *Phys. Rev. B* **93**, 245120 (2016).
47. Ueda, K. et al. Spontaneous Hall effect in the Weyl semimetal candidate of all-in all-out pyrochlore iridate. *Nat. Commun.* **9**, 3032 (2018).
48. Disseler, S. et al. Magnetic order in the pyrochlore iridates $A_2Ir_2O_7$ (A = Y, Yb). *Phys. Rev. B* **86**, 014428 (2012).
49. Shapiro, M. et al. Structure and magnetic properties of the pyrochlore iridate $Y_2Ir_2O_7$. *Phys. Rev. B* **85**, 214434 (2012).
50. Dmitrienko, V. E., Ishida, K., Kirfel, A. & Ovchinnikova, E. N. Polarization anisotropy of X-ray atomic factors and 'forbidden' resonant reflections. *Acta Cryst.* **A61**, 481–493 (2005).
51. Suzuki, M. et al. Multipole expansion for magnetic structures: a generation scheme for a symmetry-adapted orthonormal basis set in the crystallographic point group. *Phys. Rev. B* **99**, 174407 (2019).
52. Onoda, S., Sugimoto, N. & Nagaosa, N. Quantum transport theory of anomalous electric, thermoelectric, and thermal Hall effects in ferromagnets. *Phys. Rev. B* **77**, 165103 (2008).
53. Nagaosa, N., Sinova, J., MacDonald, A. H. & Ong, N. P. Anomalous Hall effect. *Rev. Mod. Phys.* **82**, 1539 (2010).
54. Chun, S. et al. Magnetic excitations across the metal-insulator transition in the pyrochlore iridate $Eu_2Ir_2O_7$. *Phys. Rev. Lett.* **120**, 177203 (2018).
55. Goswami, P., Roy, B. & Sarma, S. D. Competing orders and topology in the global phase diagram of pyrochlore iridates. *Phys. Rev. B* **95**, 085120 (2017).

Acknowledgements

The authors deeply acknowledge J. Pixley, G. Fiete, X. Hu, P. Laurell, D. Vanderbilt, D. Khomskii, H. Kim for numerous insightful discussions. X.L. acknowledges Z. Ding and H. Ren for their assistance on the transport measurements at the Synergetic Extreme Condition User Facility. X.L. and J.G. acknowledge the support by the National Key R&D Program of China (Grant No. 2022YFA1403400), the National Natural Science Foundation of China (Grant No. 12250710675, 12204521), and the Strategic Priority Research Program of the Chinese Academy of Sciences (No. XDB33000000). M.K., M.T., T.W., and J.C. acknowledge the support by the U.S. Department of Energy, Office of Science, Office of Basic Energy Sciences under award number DE-SC0022160. Y.Q. acknowledge the support by the National Natural Science Foundation of China (Grant No. 12374144). H.C. and W.H. acknowledge support from the U.S. Department of Energy, Office of Science, Office of Basic Energy Sciences Early Career Research Program under Award Number DE-SC-0021305. This research used resources of the Advanced Photon Source, a U.S. Department of Energy Office of Science User Facility operated by Argonne National Laboratory under Contract No. DE-AC02-06CH11357. The RIXS experiment and data analysis were supported in part by the U.S. Department of Energy, Office of Science, Basic Energy Sciences, Materials Science and Engineering Division. A portion of this work was carried out at the Synergetic Extreme Condition User Facility (SECUF).

Author contributions

X.L. and J.C. conceived the project. X.L. and M.K. developed the sample fabrications. X.L. performed the magneto-transport measurements with assistance from F.W. and T.W. and carried out the synchrotron X-ray magnetic circular dichroism experiments with assistance from Y. Choi and D.H. J.K., and P.R. performed the resonant X-ray scattering experiments. M.T., X.J., H.C., W.H., and Y.Cao carried out the resonant inelastic X-ray scattering experiments with assistance from M.U. and J.K. Theoretical analyses on magnetic structures were carried out by Y.W. and Y.Q. with insights from S.P. and H.W. The manuscript was written by X.L., Y.W., J.G., and J.C. All authors discussed the results and commented on the manuscript.

Competing interests

The authors declare no competing interests.

Additional information

Supplementary information The online version contains supplementary material available at https://doi.org/10.1038/s41467-024-54655-7.

Correspondence and requests for materials should be addressed to Xiaoran Liu.

Peer review information *Nature Communications* thanks the anonymous reviewers for their contribution to the peer review of this work. A peer review file is available.